

Research Article

Innovative Means of Surface Blowing towards Heat Alleviation for Hypersonic Flows

Mahmood Khalid  and Khalid A. Juhany

Department of Aeronautical Engineering, King Abdulaziz University, Jeddah 21589, Saudi Arabia

Correspondence should be addressed to Mahmood Khalid; mkholid@kau.edu.sa

Received 9 December 2018; Revised 9 April 2019; Accepted 12 June 2019; Published 5 August 2019

Academic Editor: Eusebio Valero

Copyright © 2019 Mahmood Khalid and Khalid A. Juhany. This is an open access article distributed under the Creative Commons Attribution License, which permits unrestricted use, distribution, and reproduction in any medium, provided the original work is properly cited.

A computational-based investigation has been carried out to examine the heat transfer effects of normal and tangential blowing on blunt surfaces exposed to high Mach number flows. Experimental results from such studies where a controlled outflow is imposed upon a surface under hypersonic conditions are few and far between. Simple 3D axisymmetric configurations supporting flat front surfaces suited to accommodate uniform frontal flow or round-nosed conical bodies with a stepped shoulder to provide uniform parallel flow to the conical surface were selected from a NASA experiment for validation purposes. Uniform outflow of 0.55 to 1.0 kg/s was applied in the presence of the prevailing free stream of $M = 6.8$ to assess the extent of heat transfer rate alleviation. The numerical simulation confirmed the experiment that the application of outflow in both cases leads to the surface heat transfer relief.

1. Introduction

Hypersonic vehicles experience very high heating rates near the leading edge regions. The flow has to be very carefully treated to minimize the strong shock effects by blunting the shape or using other active flow control technique near the surface to reduce the high temperature effects. It has been found that by simply blunting the leading edge geometry, it is possible to deflect the high temperature gradient towards the free stream flow but it is certainly not enough to avoid further damage from residual heating loads still present in the flow. Further active and passive means are warranted to minimize the impact. Invariably, the surface exposed to the intense heating is equipped with specially treated materials with an ability to absorb large amounts of heating loads and successfully protect the inner structures and environment from external conditions. Blowing close to the exposed surface is a well-known technique to alleviate these extreme conditions. In such applications, a very thin layer of coolant is introduced adjacent to the surface by blowing from a high-pressure reservoir inside the vehicle. This layer of cool fluid sandwiched in between the high-pressure flow ahead

of the blunt nose and the vehicle surface not only acts as physical insulation but has the effect of fattening up the underlying boundary layer leading to heat transfer rate reductions. In the present investigation, we examine two methods which employ both normal and tangential blowing to study the heating effects on the body. While it would be inappropriate to give a blow by blow account of all the heat transfer studies to date, it would be useful to mention some relevant contribution to the present investigation.

Heat transfer to surfaces of vehicles travelling at hypersonic speeds has been an area of major concern from the first design concepts. Lees's work [1] on blunt-nosed bodies in hypersonic flow laid the foundations of hypersonic heat transfer studies on axisymmetric bodies at high Mach numbers. The stagnation region which bears the brunt of the heating onslaught was tackled by Fay and Riddell [2] who provided comprehensive and well-proven formulae for calculating stagnation heat transfer rates often used for normalizing heat distribution on other surfaces. A complimentary work on heat transfer rate studies near stagnation regions of yawed cylindrical bodies was carried out by Cohen [3]. An important heat flow study of heat flow past flat plates,

cones, and blunt bodies was reported by Crabtree et al. [4]. It is equally well known that turbulent flow causes higher heat transfer rates than the equivalent laminar flow. Hypersonic vehicles often come with protective ablative shield which trigger premature transition to turbulent flow. Chen [5] predicted that such protective ablative layers can be responsible for as much as 100% increase in maximum heat transfer rates when compared to a smoother wall. More recently, Cross and Boyd [6] conducted a two-dimensional simulation of pyrolyzing materials for rocket nozzle applications by coupling the LeMANS flow solver to the MOPAR-MD material response algorithm. Zhu et al. [7] investigated numerically the drag and heat reduction induced by a lateral jet injected at the fore end of a spike using RANS equations coupled with the $k-\omega$ turbulence model. Flow patterns from mass decelerator jets normal to the frontal surface of a Mars-type aeroshell have also been described by Alkandry et al. [8] using the PLIIF technique while comparing their results favorably to CFD results using the LeMANS code.

Quite often, the shocks from the leading edge interact very strongly with an aft shock triggered by a sudden increase in slope of the body. The interacting shock systems can form a compression corner with instantaneous jump in heating rates. Experimental and theoretical work has been reported by Holloway et al. [9] and Keyes et al. [10], respectively, such heat transfer studies. Back and Cuffel [11] came up with an empirical relation between the upstream and downstream portions of the heating rates as

$$\frac{\dot{q}_{w2}}{\dot{q}_{w1}} = \left(\frac{p_2}{p_1}\right)^{0.85}. \quad (1)$$

In more recent CFD studies of shock interaction-based heat transfer studies, Candler et al. [12] provide a number of cases used for validating the complex physics in the shock boundary layer interaction region. Here at King Abdulaziz University, Pasha et al. [13] have tried to improve upon the one-equation Spalart-Allmaras turbulence model by accounting for the shock unsteadiness to simulate heat transfer rates in the compression corner.

In terms of heat transfer rate reduction through surface blowing, some of the earlier studies were reported by Howe and Mersman [14] for transpiration cooling and by Low [15] for cooling studies on flat plates placed in supersonic flow. It was, however, the classic work by Pappas and Okuno [16, 17] that was able to quantify the effects of injectants heavier and lighter than the air. The correlation studies for laminar and turbulent flows leading to heating rates with respect to the stagnation point and depending upon the molecular weights of injectant and free as stated by Dorrance [18] are as follows:

$$\psi \equiv \frac{\dot{q}_w}{\dot{q}_{wb=0}} \equiv \frac{\text{heat transfer rate}}{\text{heat transfer rate without blowing}}, \quad (2)$$

$$\psi = 1 - a \left(\frac{M_e}{M_w}\right)^n B + b \left(\frac{M_e}{M_w}\right)^{2n} B^2,$$

where a , b , and n are specific constants for the stagnation points, flat plate, or a conical surface. M_e is the molecular weight of the gas in the shock layer, and M_w is the molecular weight of the injected gas. B is the mass rate parameter = $(\dot{m}_w/\dot{q}_{wb=0}) [h_{oe} - h_w]$, and \dot{m}_w is the mass flow rate of the injected gas. For an in-depth and detailed discussion on the above heat transfer methodologies, see Tauber [19].

As alluded to earlier, in the present heat transfer rate study, two configurations were central to this investigation.

- (i) In the first configuration (Figure 1), the outflow was applied normal to the flat nose surface of an axisymmetric conical body named as the Gasjet model
- (ii) In the second configuration (Figure 2), the circumferential outflow is applied tangentially to the conical surface from a shoulder just past the blunt nose of the conical axisymmetric body called the tangent-slot model

Complimentary computations were performed on two further solid baseline spherically blunt nose cone models R1 and R3 which corresponded in geometry to the above two central configurations. The results were systematically examined against the measurements provided by Nowak [20] on the above two primary configurations of interest and the two solid blunt nose axisymmetric configurations included as baseline models.

2. Computation Methodology

The conservative form of the compressible Reynolds-Averaged Navier-Stokes equations in the in-house algorithm are as follows:

$$\begin{aligned} \frac{\partial \rho}{\partial t} + \frac{\partial [\rho u_j]}{\partial x_j} &= 0, \\ \frac{\partial}{\partial t} (\rho u_i) + \frac{\partial}{\partial x_j} \left[\rho u_i u_j + p \delta_{ij} - \left(1 + \frac{\mu_t}{\mu}\right) \tau_{ij} \right] &= 0, \\ \frac{\partial}{\partial t} (\rho E) + \frac{\partial}{\partial x_j} \left[\rho u_j E + u_j p - \left(1 + \frac{\mu_t}{\mu}\right) u_i \tau_{ij} - \left(c_p \frac{\mu}{Pr} + c_p \frac{\mu_t}{Pr_t}\right) \frac{\partial T}{\partial x_j} \right] &= 0, \end{aligned} \quad (3)$$

where ρ in these equations refers to the density, p is the pressure, and T is the temperature. E is the total energy, and u is the velocity vector in tensor format. τ_{ij} is the viscous stress tensor which may be written as

$$\tau_{ij} = \mu \left(\frac{\partial u_i}{\partial x_j} + \frac{\partial u_j}{\partial x_i} - \frac{2}{3} \frac{\partial u_k}{\partial x_k} \delta_{ij} \right). \quad (4)$$

The above Navier-Stokes equations, formulated in strong conservation form to be used in the structured meshes of the present study, are first cast into curvilinear coordinate scheme following the Vinokur transformation method [21]. The numerical algorithm used to solve the Navier-Stokes equations is an implicit factorization finite center difference

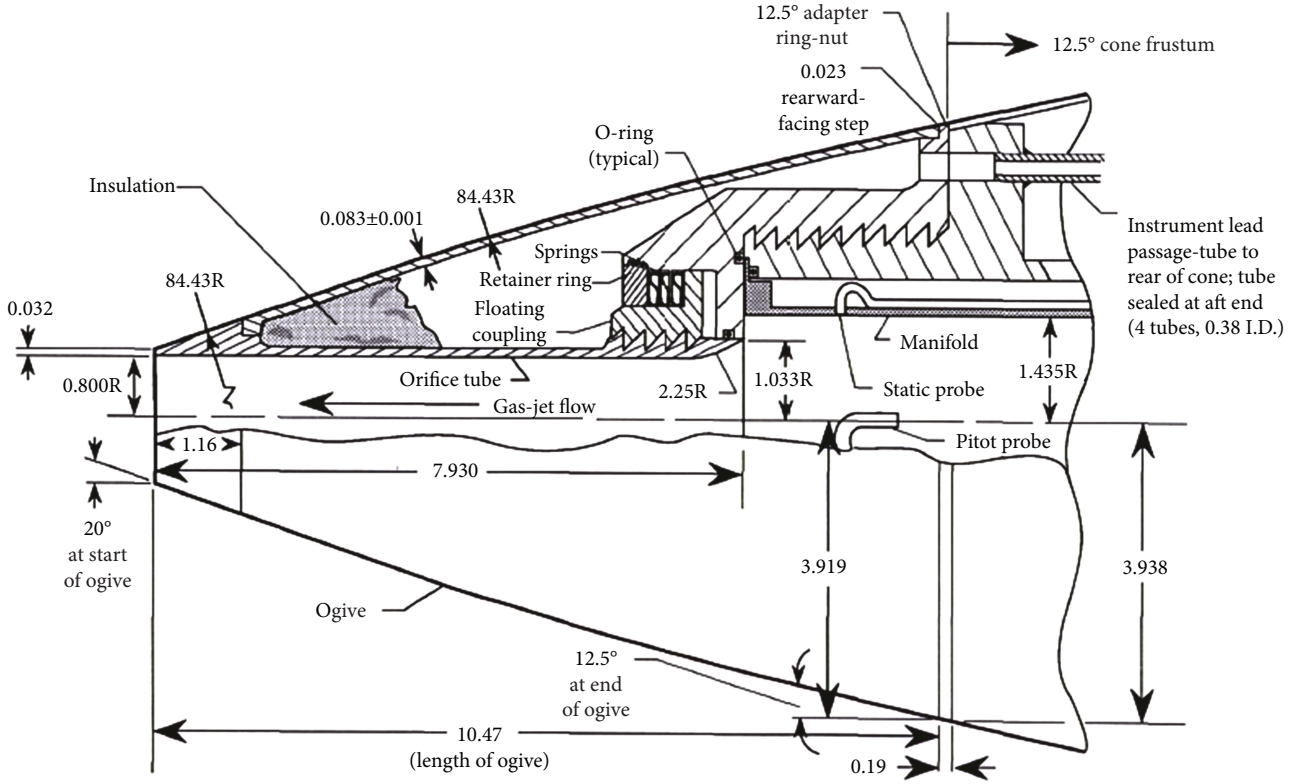


FIGURE 1: Gasjet frontal blowing model, Nowak [20].

scheme about a regular rectangular prism which is described at length by Beam and Warming [22]. Local time linearization is applied to the nonlinear terms following Pulliam and Chaussee [23]. Approximate factorization scheme is applied to the resulting matrices which factorizes the operator itself resulting in efficient matrix equations with narrow bandwidth. This results in block tridiagonal matrices which are easy to solve. The spatial derivatives can thus be approximated using second-order central differences. Explicit and implicit artificial dissipation terms are added to achieve nonlinear stability. A spatially variable time step is used to accelerate convergence to steady state solutions. The algorithm can be used to solve time accurate or steady state flow problems.

The fact that the Navier-Stokes equations are formulated in a strong conservation form as well as the implicit treatment of the artificial dissipation and the inclusion of a second-order dissipation terms helps in the shock capturing at high Mach numbers.

We selected $k-\epsilon$ and the Wilcox $k-\omega$ turbulence models for this investigation. For the two equation turbulence models, the convection and diffusion terms of their transport equations are negligible in the inertial sublayer so that local equilibrium prevails, which implies that the production of the turbulent kinetic energy k is equal to the dissipation rate. The local equilibrium condition leads to two simple relations which can be used as boundary conditions for k and the dissipation terms for both incompressible and compressible flows. The compressible wall functions as explained by Zhu and Shih [24] have been successfully applied to

both attached and separated flows under Mach number ranging from 0.1 to 10.

While the purpose in this study was not to scrutinize the capabilities of the turbulence models, nevertheless for these simple bodies, very little difference in results was observed from the two turbulence models. The Sutherland law is implemented to compute the laminar viscosity coefficient (μ). Since the flows computed involve hypersonic Mach number, the choice of the Prandtl number is selected to suite the Mach number whereas the use of specific heat and the specific heat ratio c_p/c_v (γ) in the algorithm for one gas species must also respect the high Mach number flow conditions subject to the relations by Grundmann [25] and Gordon and McBride [26]:

$$c_v(T) = R \left(\frac{5}{2} + \frac{(h\nu/kT)^2 e^{h\nu/kT}}{(e^{h\nu/kT} - 1)^2} \right),$$

$$c_p(T) - c_v(T) = R, \quad (5)$$

$$\frac{c_p(T)}{R} = \sum_{n=0}^{n=4} a_n T^n,$$

where T is the temperature, R is the real gas constant, h is Planck's constant, ν is the fundamental vibrational frequency, and k is Boltzman's constant and where a_n are curve-fit constants. As explained in Khalid and Juhany [27], the input flow conditions (ρ , ρu_i , and E) for the outflow surface are treated like a new "slip" condition which remains

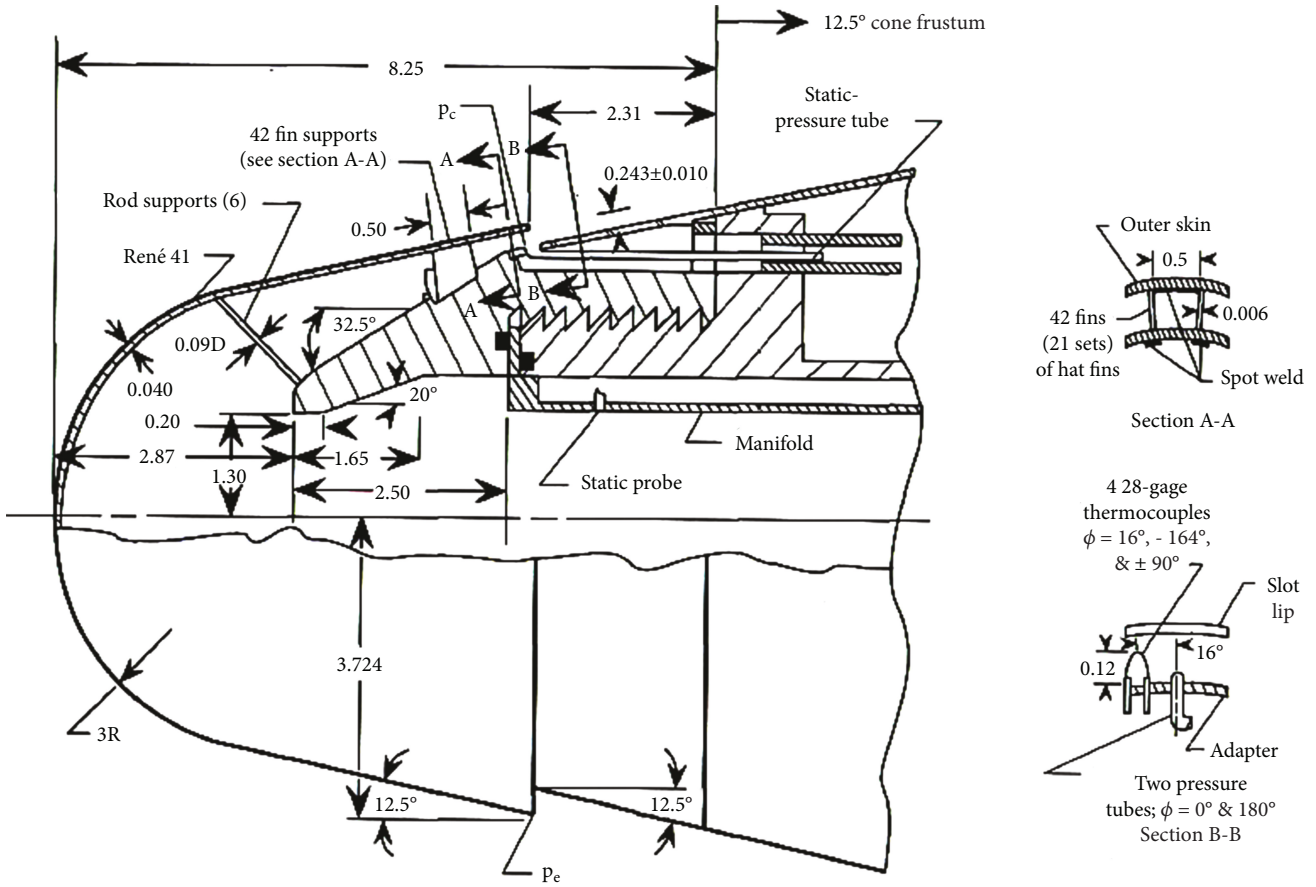


FIGURE 2: Tangent-slot blowing model, Nowak [20].

fixed during the flow applied run. The algorithm iterates between the successive grid planes near the exit control boundary until the desired flow conditions are matched at the exit boundary as the convergence criterion is reached. For the corresponding solid surface run, this surface would understandably carry a no-slip boundary condition. Since the present applications of the code deals with axisymmetric flow fields produced when a simple two-dimensional mesh is rotated about the body axis through a 45° azimuthal angle, the flow has to be carefully treated near the polar stations. In such cases, a computational coordinate surface may represent a physical 3D line. For example, with an “O” grid, the circles (2D) or cylinders (3D) collapse to points and lines, respectively. The flow variables at the singular boundary are the average of the points surrounding the singular point.

3. Simulation Models

CFD simulations were carried out on four configurations. The two baseline blunt-nosed conical models R1 and R3 from Nowak [20] are simple 3D axisymmetric configurations with tip bluntnesses of 1 in (25.4 mm) and 3 in (76.2 mm) with respect to the complete model of base diameter 36 in (914.4 mm) supporting interchangeable nose tips. While the baseline model R3 is used for more detailed axial flow field comparisons, the stagnation heat flux of the baseline model

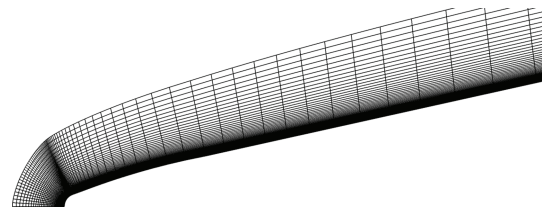


FIGURE 3: R1 model, mesh size (75,120,90).

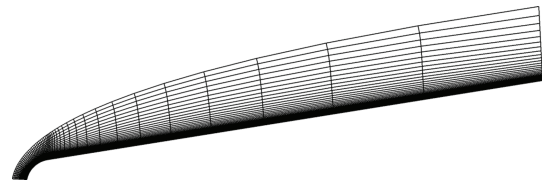


FIGURE 4: R3 model, mesh size (75,120,90).

R1 is used for nondimensionalizing the local heat transfer value, *q* for all the models. The two surface blowing models with frontal and tangent-slot blowing models were also mounted upon the same aft support. The four configurations are shown in Figures 3–6.

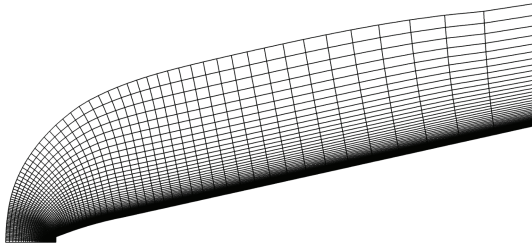


FIGURE 5: Gasjet model, mesh size (75,120,90).

For the baseline models R1 and R3, the viscous nonslip boundary condition was imposed on the solid surface with far upstream condition input as far upstream at front and at the far azimuth direction. These freestream flow conditions are calculated using the incidence, yaw and Mach number. The nondimensional pressure and temperature correspond to static free stream conditions. An extrapolation boundary condition was applied at the far downstream end. In the extrapolation case, the conditions at the boundary are approximated to be the same value as one point off this boundary using zero differential. It should be noted that consistent with our earlier studies [28] on complex hypersonic configurations, the y^+ value for the meshes used in the present investigation was kept very close to 1. Dedicated grid convergence studies (results not shown for brevity) were carried out to assure that the final grid selected provided the most accurate and best converged solution. In the case of the R3 model, for example, four grids of dimensions from (75,90,90) to (75,120,90) were executed in turn until no further accuracy could be achieved by further increase of grid lines in the normal direction.

For the no-outflow cases on the Gasjet and the tangent-slot models, all the far field and solid surface boundary conditions were the same as the solid baseline models R1 and R3. For the outflow case on the Gasjet model, all other boundary condition on the solid surface and the far boundaries remained the same as the no-outflow case except at the flat frontal nose where a new (u , ρu_j , and E) flow conditions corresponding to the outflow transpiration was imposed on the boundary.

Figure 6(b) shows the boundary topology of the tangent-slot model comprising of two meshes abutting at the common boundary. An abutting contiguous boundary scheme was used to pass the flow from Block 1 to Block 2 at the joint boundary. In Block 2, as many as 30 grid points in a direction normal to the surface were reserved for the shoulder and the remaining 90 points abutted the end surface from upstream Block 1. These 30 points were equipped as a no-slip boundary for the no-flow case and carried the jet flow condition for the flow-on case. In this case, for the tangent-slot model, the outflow condition was imposed on the circumferential jet at the shoulder. The jet emanated parallel to the conical surface.

All blunt noses R1, R3, Gasjet, and tangent slot that have the same base diameter of 7.875 are mounted on the same cone frustum of the inner and outer diameters of 7.875 in and 36.00 in. In order to standardize their axial distances, the origin of all the models was determined to exist at a point

where the generators of the frustum meet (Nowak [20]). The distance S_a was then measured from this origin allowing for the variation of the geometry at the nose.

The jet condition was evaluated from the jet $(\rho u)_{jet}$ and (ρu_{jet}^2) tabulated in the experiment and jet mass flow rates in Nowak [20]. Knowing the flow total temperature and the free stream Mach number, the free stream velocity and ρ_{∞} can be evaluated from the Reynolds number assuming a value of the viscosity, μ_{∞} . Thus, nondimensional ρ/ρ_{∞} , $\rho u/\rho_{\infty} u_{\infty}$, and e is then readily calculated as an input for the outflow boundary condition.

4. Discussion of Results

4.1. Computations for the Models R1 and R3. The flow past the blunt baseline models R1 and R3 was calculated first to test the capabilities of the code for solving hypersonic blunt body problem. The flow field Mach number distributions over models R1 and R3 are shown in Figures 7 and 8, respectively. As expected, the shock wave surrounding the blunt models is stronger and sharper near the nose regions where the entropy gradient is strong and is more smeared away from the nose towards the conical surfaces. The temperature contour lines are indicative of how accurately the shock is captured within the flow field. The presence of continuous temperature contours and their coalescence close to the shock, in both Figures 7(b) and 8(b), confirms that the strong shock near the blunt nose is captured quite effectively in the high-pressure region. Away from the blunt nose, in both cases, the shock is quite smeared and the temperature contours show notable deviations near the shock region before they assume a more continuous behavior in the flow field close to the body.

Total enthalpy for the models R1 and R3 was also recovered in the form of percent error $(ht/ht_{\infty} - 1)\%$ from the computed flow fields. Figures 9 and 10, respectively, show this percent error for both models R1 and R3, respectively.

To analyze the flow field a little more closely, the percent error was examined along the lines of the analysis by Kirk [29]. Towards this end, percent total enthalpy error was calculated along a normal $k = 92$ from the surface and along the mesh axial generator j for both models. The mesh line along which this enthalpy percent error was carefully chosen so that it starts from the total stagnation line just ahead of the nose and traverses across the shock in the strong shock region and moves axially towards the length of the body. The line along which the percent error is clearly visible is shown in Figures 9 and 10. The total enthalpy percent error for both models is shown in Figure 11.

Both models show a drop in total enthalpy error close to the shock. For model 1 which has lower bluntness experiences, there is a drop of about 5% whereas the blunter model experiences a less severe drop in error of 4%. Past the shock wave of the flow field, the error remains less than 1%. It was observed in Figure 12 that the application of the two turbulence models produced almost identical flow field on the R3 model, and only one result from the $k-\omega$ model is shown. The pressure distribution is compared

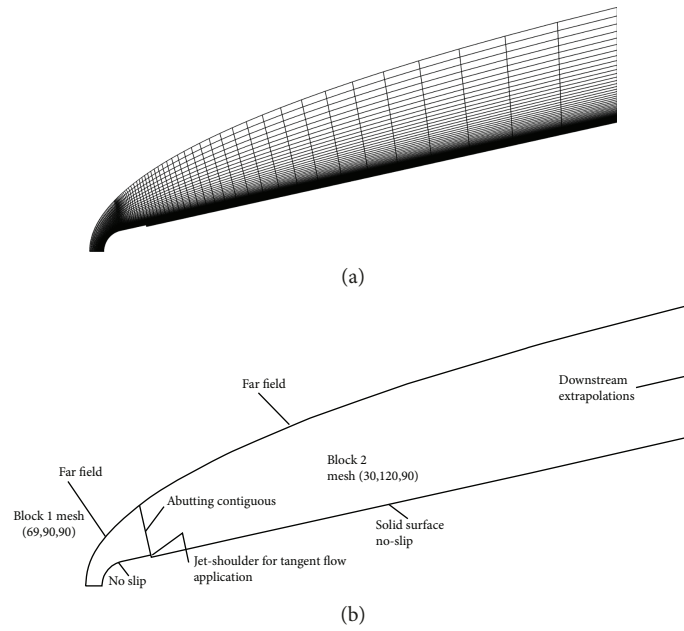


FIGURE 6: Tangent-slot model (a) mesh block 1 (69,90,90), mesh block 2 (30,120,90). (b) Topology showing boundary conditions.

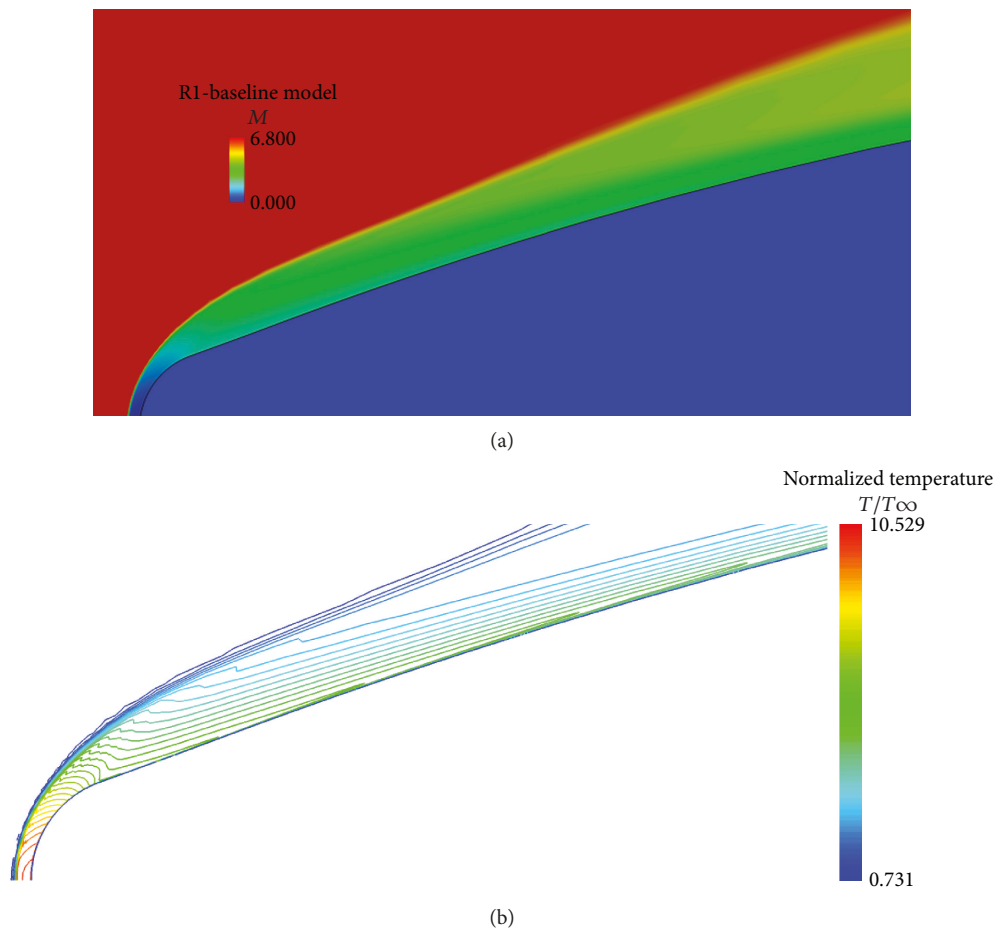


FIGURE 7: (a) Model R1, Mach number distribution, $Re = 4.4 \times 10^6$, $\alpha = 0.0^\circ$, $M = 6.8$. (b) Model R1, normalized temperature, $Re = 4.4 \times 10^6$, $\alpha = 0.0^\circ$, $M = 6.8$.

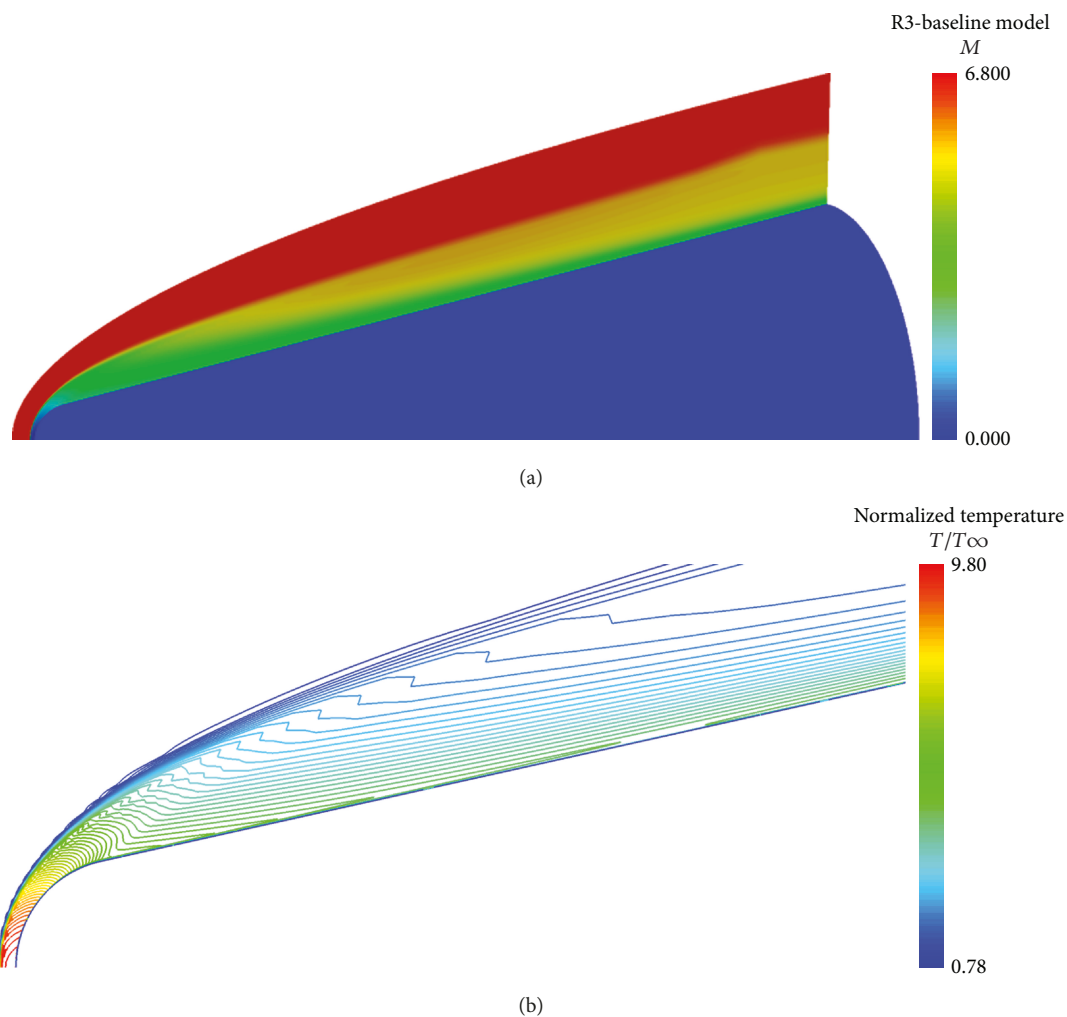


FIGURE 8: (a) Model R3, Mach number distribution, $Re = 4.4 \times 10^6$, $\alpha = 0.0^\circ$, $M = 6.8$. (b) Model R3, normalized temperature, $Re = 4.4 \times 10^6$, $\alpha = 0.0^\circ$, $M = 6.8$.

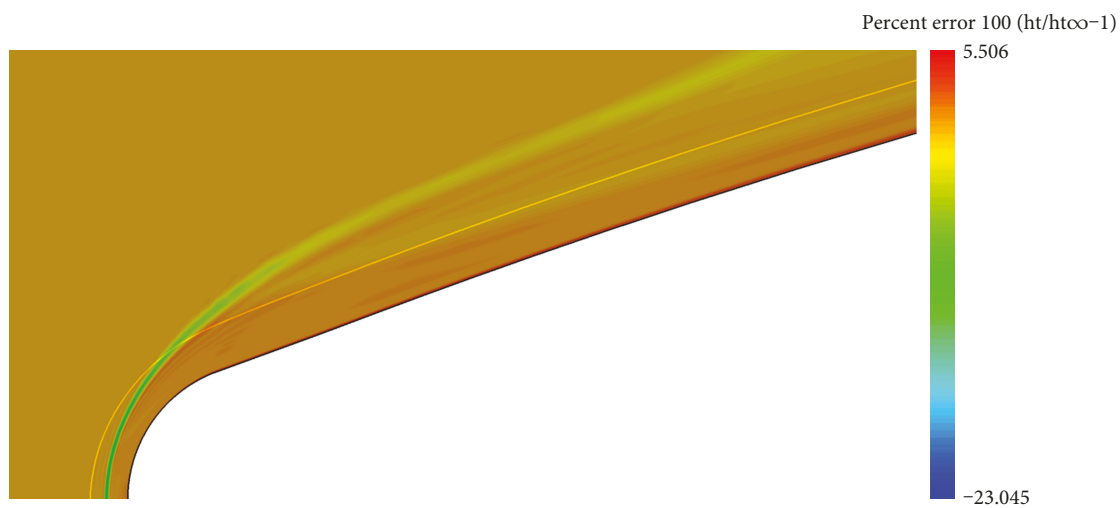


FIGURE 9: Total enthalpy percent error $(ht/ht_\infty - 1)\%$ (model R1).

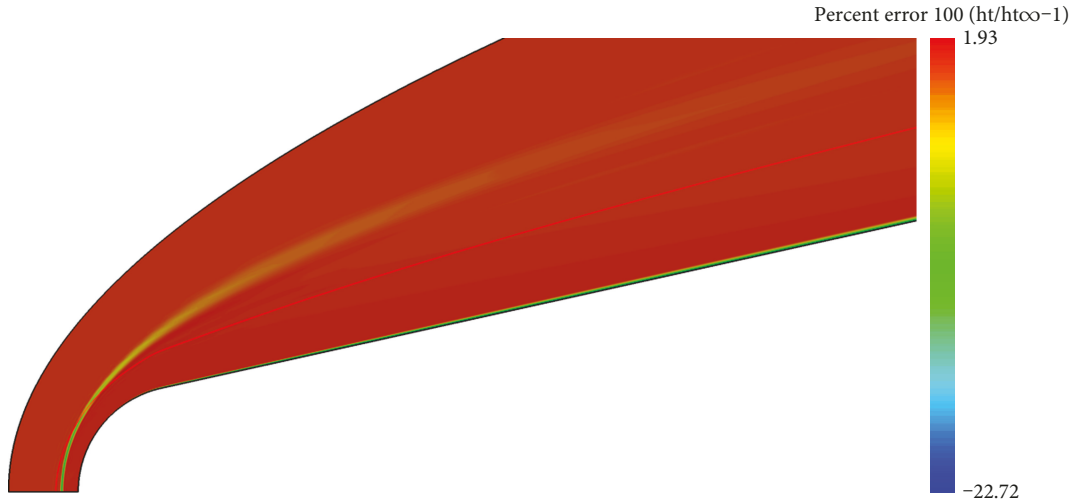


FIGURE 10: Total enthalpy percent error (ht/ht ∞ - 1)% (model R3).

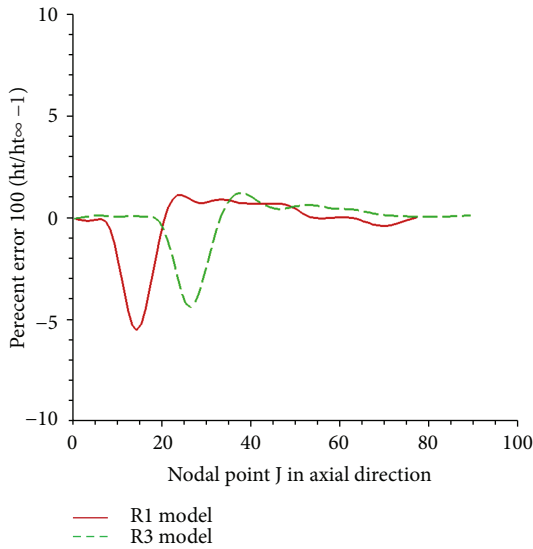


FIGURE 11: Total enthalpy % error at a normal station $k = 92$ from the surface.

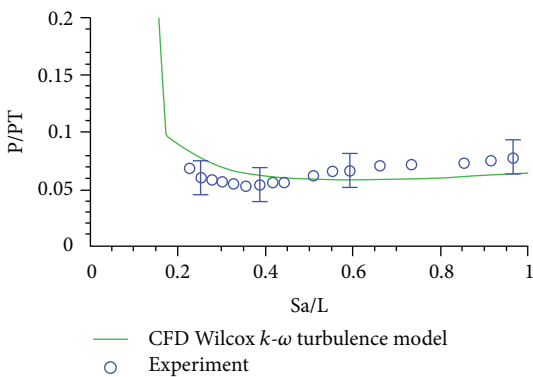


FIGURE 12: Pressure distribution on model R3.

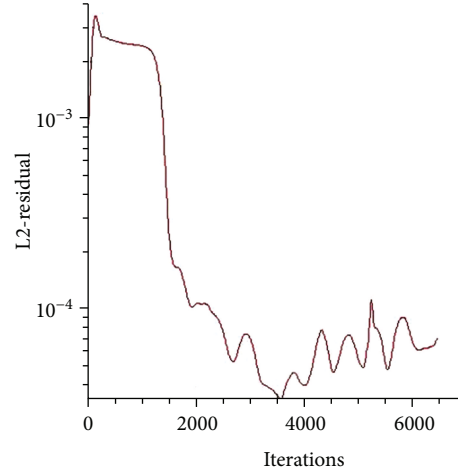


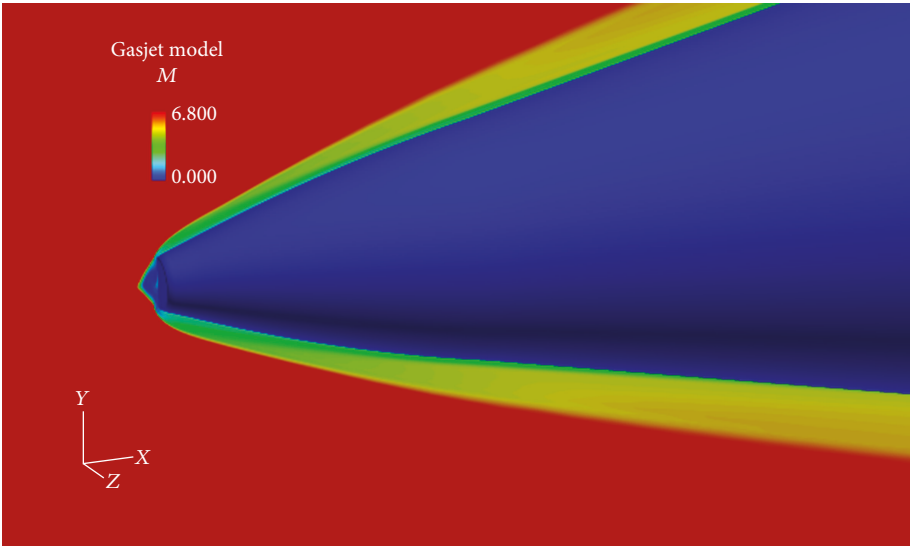
FIGURE 13: L2-residual convergence history of the solid Gaset model.

against the measurements from Nowak [20]. While the results from the two models matched almost exactly with each other, yet they were not able to resolve the expansion region when compared with the experiment. Almost the same type of results were obtained on R1.

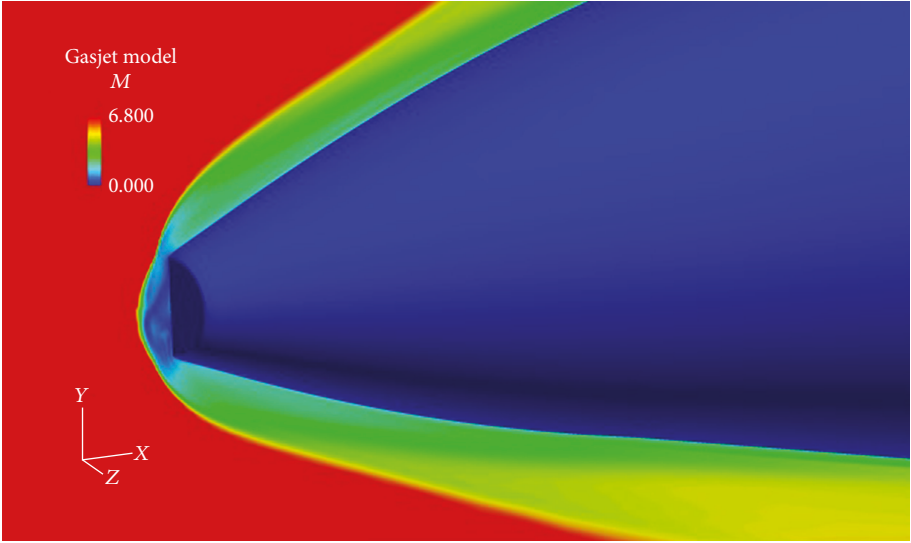
5. Computations for the Gaset Model

As observed from the solution convergence history in Figure 13, the computation past the Gaset model particularly near the nose region was numerically unstable.

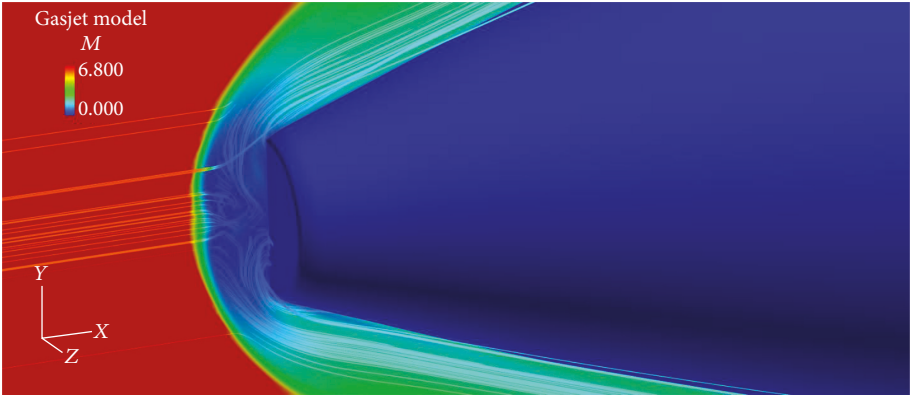
Unexpectedly, a single converged solution (a fixed flow configuration) was not obtained, even with two orders of L2 residual convergence; successive solutions as depicted by Figures 14(a)–14(c) were obtained. In Figure 14(a), the flow reflecting from the flat surface at the nose is not immediately swept downstream as typically observed in the flow past round tips. Instead, it interacts very strongly against the



(a)



(b)



(c)

FIGURE 14: Solid Gasjet model during different stages towards final convergence.

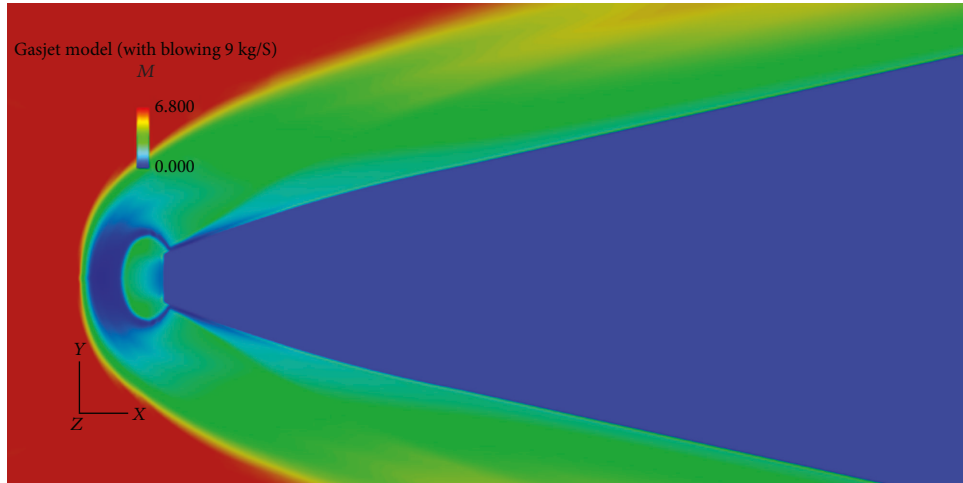


FIGURE 15: Gasjet model, blowing at flat nose 0.91 kg/S, $Re = 4.3 \times 10^6$, $\alpha = 0.0^\circ$, $M = 6.8$.

incoming flow emerging from the leading shock, penetrating further upstream resulting in a numerically unstable flow. The shock shape at the start of this destabilizing process is similar in appearance to the one created in a flow over a spiked nose that gradually approaches the expected rounded bow shock configuration, typical of hypersonic flow over blunt nose. It then deforms again into a conical configuration before converging towards the bow shock shape again. This has been picked up by the oscillations in the residual history curve in Figure 13. This “numerically unsteady” flow phenomenon is most likely caused by the carbuncle instability as observed by Peery and Imlay [30], Ismail and Roe [31], and Garicano-Mena et al. [32]. The occurrence of carbuncle instabilities has been attributed to numerical finite difference upwind schemes, computational rounding off errors, and instabilities in convective terms of the Navier-Stokes equations. While the steady solutions did not blow up, it continued to capture a numerically oscillating flow field brought about by an inherent numerically unsteady flow. The solution for present analysis was carefully selected when the fully detached well-formed rounded shock persisted for at least 300 iterations. Figure 14 shows the evolutionary stages of the “unsteady” shock formation immediately upstream of the flat surfaced Gasjet. The streamlines in Figure 14(c) confirm that the flow from the flat surfaces reverses and interacts with the oncoming flow from the shock.

In the case of the outflow application from the flat surface at the nose, the convergence was much slower. Starting from an earlier solid surface no-outflow solution, it took another 4000 iterations to obtain the same level of convergence. A typical solution from an outflow case on the Gasjet model is shown in Figure 15, together with the experimental results from Nowak [20] in Figure 16. Both computations and the shadowgraph confirm that the outflow at the nose causes the stagnation region to be blown outwards in a spherical bubble shape pushing against the frontal shock. Note the presence of the supersonic bubble inside of the main shock. The flow region in between the main jet interface and the nozzle shock contains the slower expanded flow in both simulation and the experiment.

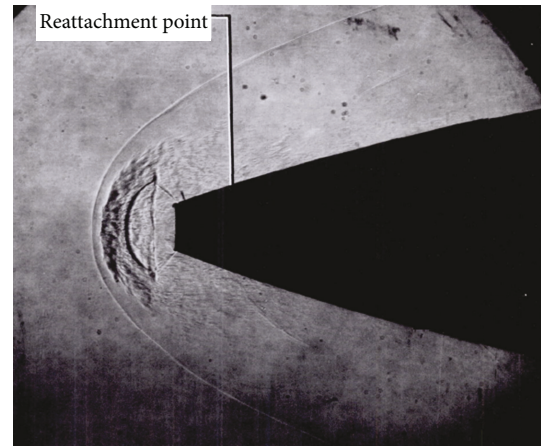


FIGURE 16: Gasjet experiment, blowing at flat nose 0.91 kg/S, $Re = 4.3 \times 10^6$, $\alpha = 0.0^\circ$, $M = 6.8$, Nowak 1988.

It was also observed by plotting velocity vectors near the nose on the top surface that the flow ejection at the nose invokes separation of the flow at the top lip and causes a circular redirection of the main flow from the stagnation region outwards which then comes back to impinge upon the model at a distance of about 3 nose radii from the lip forcing a flow attachment. The flow velocity vectors are shown in Figure 17. It can be seen that similar to the experiment, the flow is reattached at a distance of about 3 flat nose radii downstream from the lip.

The flow field from computations was first validated for pressure distributions obtained on the Gasjet model as well as the earlier baseline models against the measurement from Nowak [20].

The pressure distribution results in Figure 18 show that the computed results for the solid surface models and even for the lower outflow (0.55 kg/s) Gasjet model agree well with the experiment. It must be noted that the surface pressure along the solid flat nose must decrease from the stagnation

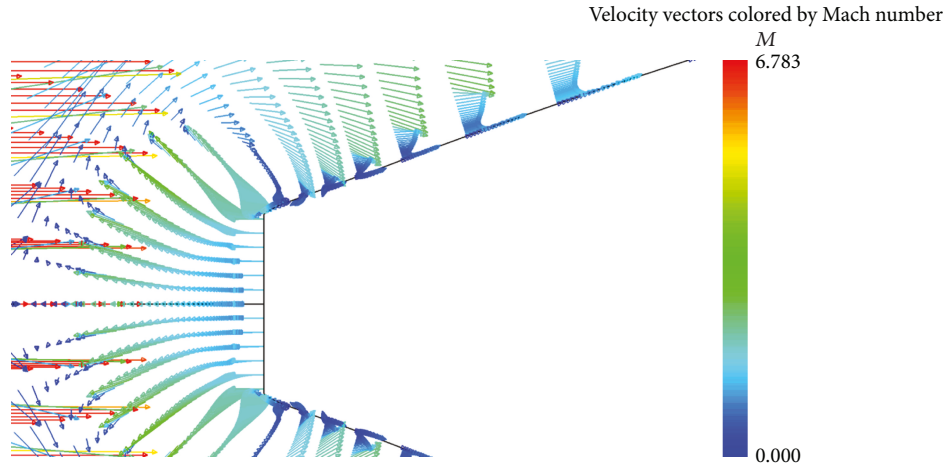


FIGURE 17: Gasjet model, blowing at flat nose 0.91 kg/S, $Re = 4.3 \times 10^6$, $\alpha = 0.0^\circ$, $M = 6.8$.

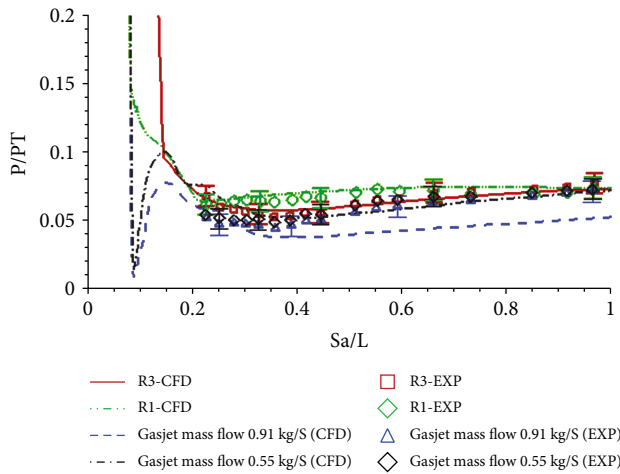


FIGURE 18: Pressure distribution on Gasjet and baseline models, $Re = 4.3 \times 10^6$, $\alpha = 0.0^\circ$, $M = 6.8$.

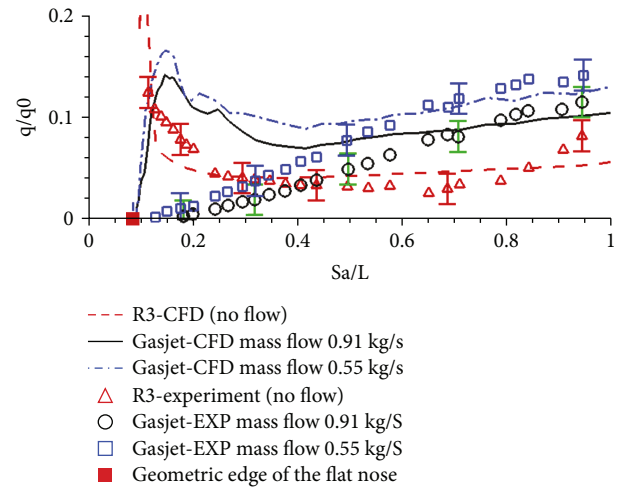


FIGURE 19: Heat transfer results of the Gasjet model against the baseline model and experiment, $Re = 4.3 \times 10^6$, $\alpha = 0.0^\circ$, $M = 6.8$.

point along the surface towards the lip as the flow expands around the corner. Thus, the total internal pressure inside of the Gasjet model would have to be specifically profiled along the flat surface to provide the constant outflow at the flat nose. The boundary conditions at the flat nose can only cater for constant outflow at the nose without reference to the applied changing pressure profile used in the experiment. The boundary condition applied at the outflow surface does not cater for applied varying pressure condition. Thus, it is understood that there will be some difference between computed and measured pressures at the flat nose. This difference in applied pressure profile at the front boundary and the computed pressure will also affect the heat transfer rates. This discrepancy with the larger blowing must also stem from the larger separation at the nose which is not as well resolved by the Wilcox $k-\omega$ turbulence model used in this calculation. Otherwise, the agreement amongst the computed results for the baseline models R1 and R3 and the low outflow case and the experimental data on the conical surface for these attached flows is quite satisfactory.

The above shortcoming of the turbulence model to resolve hypersonic separated flow must be borne in mind when analyzing the heat transfer results for the Gasjet model shown in Figure 19. In order to explain the differences in computed and measured heat transfer rates, it must be emphasized here that the regions where the flow experiences large scale separation accompanied with flow reversal, the current two equation models as observed by Khalid et al. [33] cannot resolve the flow accurately even at supersonic Mach numbers. At hypersonic Mach numbers, the challenge to derive heat transfer rates become even more difficult as the temperature gradients at the wall become extremely sensitive to underlying flow fields. An error in local pressure and density gradients will immediately magnify error in the temperature field. The challenge is all the more difficult when there is an underlying moving boundary flow instead of a bounded wall with negligible diffusion effects. When all this is interpreted in the presence of an applied pressure profile at the ejection surface, the problem becomes even more complex.

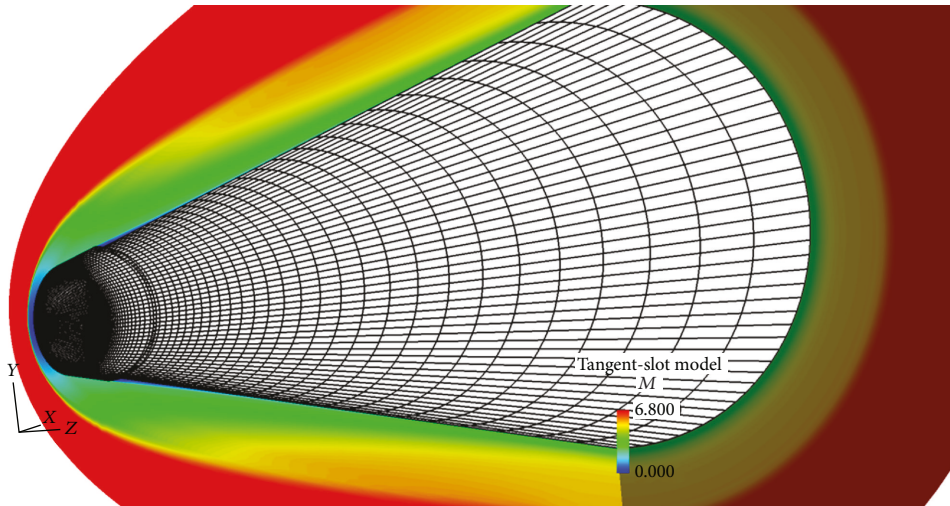


FIGURE 20: Tangent-slot model, no jet flow in the slot, $Re = 4.3 \times 10^6$, $\alpha = 0.0^\circ$, $M = 6.8$.

Towards this end, only turbulence model $k-\omega$ was used for the purpose of closing the Navier-Stokes algorithm to assess the heat transfer effects without comparing results with any other turbulence model. When a simple laminar flow was considered even on a complex vehicle (see Khalid and Juhany [27]) configuration, the present approach had provided more encouraging results. It is clear from Figure 19 that the baseline model R3 which largely support an attached flow shows high transfer rates immediately following the stagnation point which understandably supports a cooler stagnated flow. The peak loading then settles down to uniform heating flux at the conical surface followed by an increase in enthalpy as the flow exchanges heat with the high-energy free stream. This trend is well picked up by the present computations. The computed Gasjet model results also show a low heat transfer rates at the flat region followed by large heat transfer rates near the corner. Past the corner point, where the above velocity vectors had shown a notable region of flow reversal and separation, the present heat transfer results show a steady decrease before they begin to grow towards the trailing edge. The larger mass flow (0.91 kg/S) at the front always produce a lower heat transfer compared to the lower mass flow at the front jet (0.55 kg/s). While the agreement with experiment gets better towards the trailing edge, there is a noticeable difference in the region near the stagnation region and on the front surface supporting flow reversal and separation. It might be of interest to note here that Thompson and Gnoffo [34] had found very similar differences between their results and experiment near the stagnation region. It is possible that the two equation models used in the present investigation have been well calibrated with the experiment for the performance of such aerodynamic properties as pressure, velocity fields, and other shear stress distribution in routine turbulent flows. The production or dissipation of energy which is under high-temperature regimes with rotational and separating flows will include vibrational and dissociative modes, which are not accounted for in these two turbulence models. It was therefore observed that for attached flows past the blunt-nosed R3 model, the results near the stagnation region were comparatively better than the corresponding

results supporting reversing separated flows close to the flat nose of the Gasjet model.

6. Computation for the Tangent-Slot Model

The flow past the tangent-slot model was simulated using two blocks: the front block which represents the flow in the blunt nose region and also accommodated the jet slot at the bottom of the line abutting the aft conical frustum to represent the hind portion of the model. The computations were first conducted without applying any tangent slot flow in order to examine the flow patterns in the vicinity of the blunt nose. The flow field past the tangent-slot model is shown in Figure 20 with a close up of the model near the slot in Figure 21.

Without the jet applied to the slot region of the tangent-slot model, it is seen that the shoulder produces a reversing flow near the shoulder region which gains some energy from the mainstream through mixing and starts to move towards the trailing edge. The flow near the round nose region is comparatively smoother than the flow observed for the Gasjet model where the presence of carbuncle instabilities inhibit progressive convergence. The convergence in this case is thus notably faster than the convergence observed for the Gasjet model.

When the ejection flow is applied in the shoulder region, as seen in Figure 22, the flow field is transformed from having reverse and stagnant flow in front of the jet (Figure 21) to a more energetic flow layer adjacent to the wall which helps in heat alleviation in this region. However, the presence of a retarded shear layer of flow sandwiched in between the jet flow and the main flow pervades across the entire length of the model would cause some unwanted dissipation from momentum differential between the shear layers. This shear layer depicted by a blue region above the model surface will introduce unwanted velocity and temperature gradients in an otherwise uniform flow. In an ideal situation, the shoulder jet should be sufficiently strong to blend seamlessly with the main flow. It should, however, be recalled that in comparison, the flow past the flat-nosed

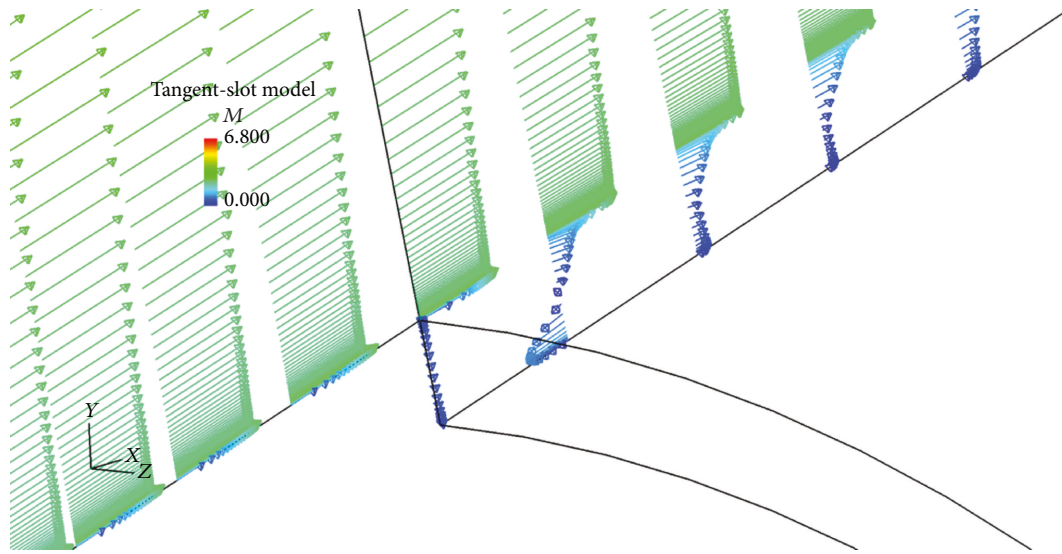


FIGURE 21: Velocity vectors near the slot region, no jet, $Re = 4.3 \times 10^6$, $\alpha = 0.0^\circ$, $M = 6$.

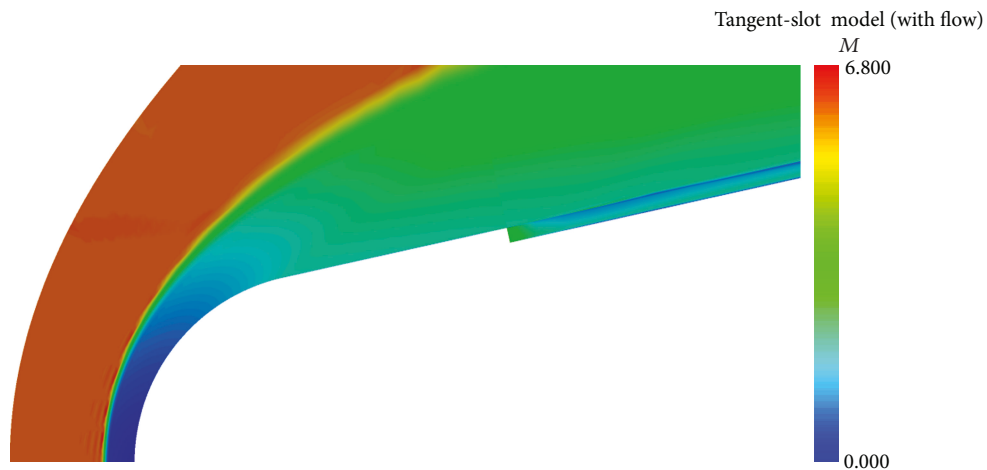


FIGURE 22: Tangent-slot model Mach number distribution, mass flow 0.55 kg/S , $Re = 4.3 \times 10^6$, $\alpha = 0.0^\circ$, $M = 6.8$.

Gasjet model is thus inherently different from the flow past the present tangent-slot model. The rebounding flow from the flat-nosed model coupled with instantaneous separation from sharp tips followed by reversing flows will aggravate heating in comparison to the smoother flow off the round-nosed tips.

The velocity vectors of the same flow field with the mass flow as shown in Figure 23 show none of the reversing flow which prevailed aft of the shoulder in the above no-outflow case. The velocity vectors also depict that there is a great deal of mixing taking place between the higher energy layer adjacent to the wall and the main stream. The normalized temperature in the flow field is shown in Figure 24. The hot regions are clearly indicated near the front immediately downstream of the strong shock. Away from this region and just past the front block, the temperature field is more diffused while the ejector jet indicates cooler temperatures in the boundary layer adjacent to the surface, but heat

transfer effects are of course based on temperature gradients rather than the local temperature conditions.

The pressure distributions from the computed results obtained from the tangent-slot model and the baseline model computations and the measurement are shown in Figure 25.

The regions on the conical surface where the pressure distribution results are available; the match between experiment and computed results is quite satisfactory. The R3 baseline model understandably shows a peak of results close to the stagnation region. The computations on the tangent-slot model show a sharp drop in the junction region which of course could not be validated as there was no data available for the region upstream of the junction point. It is clear that the application of the jet from the shoulder reduces the pressures on the circumferential surface when compared to the R3 model with the same blunt nose.

The heat flux results for the tangent-slot model along with the baseline model are shown in Figure 26. Except for

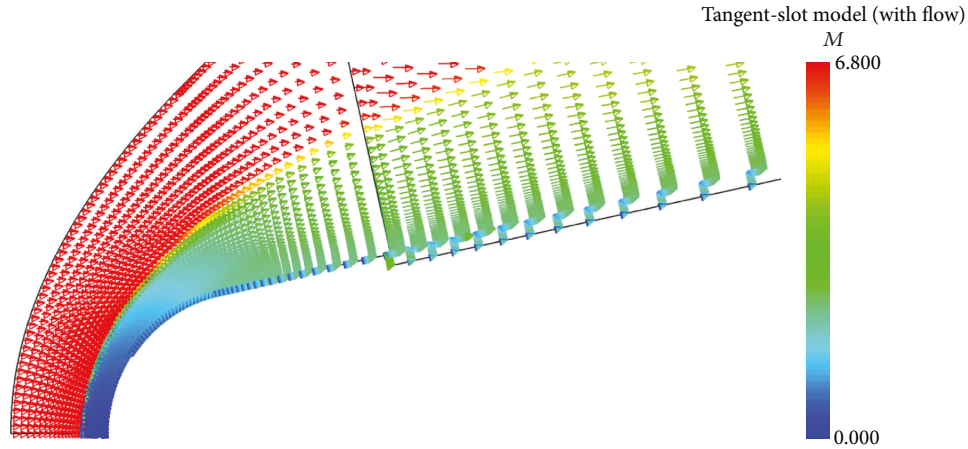


FIGURE 23: Tangent-slot velocity vectors, mass flow 0.55 kg/S, $Re = 4.3 \times 10^6$, $\alpha = 0.0^\circ$, $M = 6.8$.

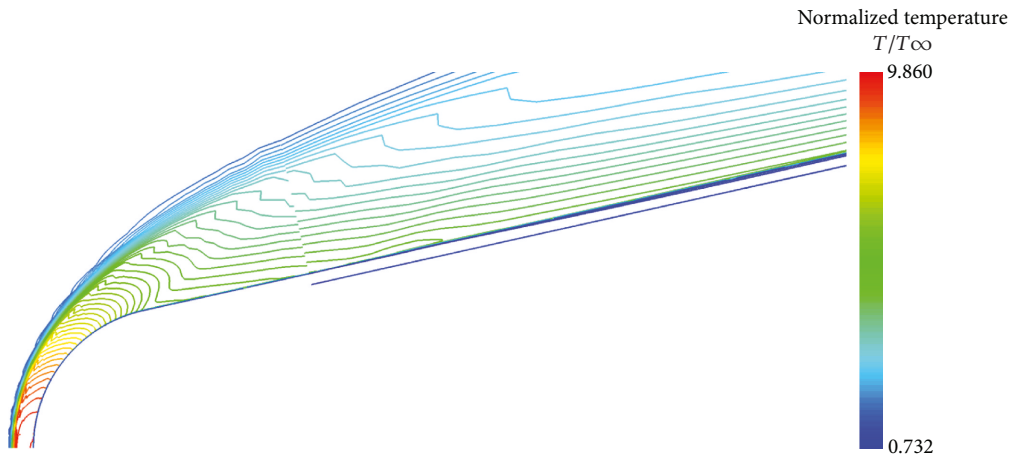


FIGURE 24: Normalized temperature, mass flow 0.55 kg/S, $Re = 4.3 \times 10^6$, $\alpha = 0.0^\circ$, $M = 6.8$.

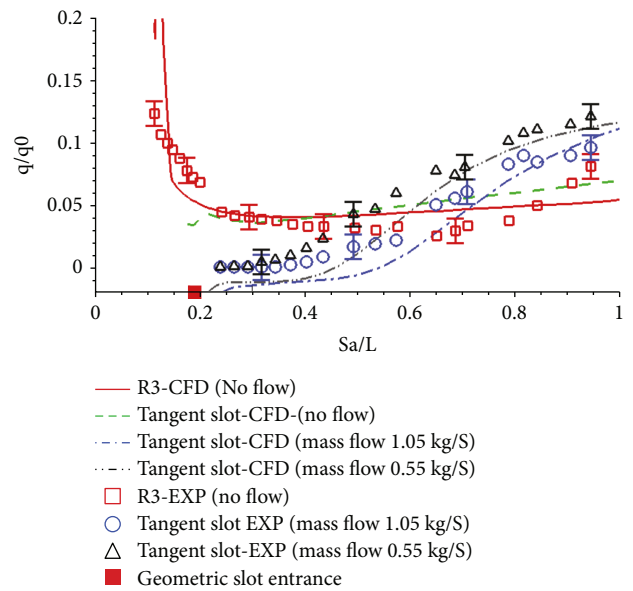
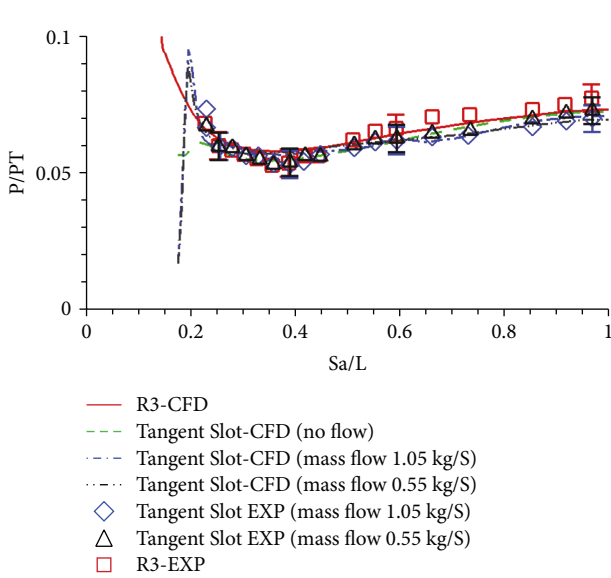


FIGURE 25: Pressure distribution on the tangent-slot model and the baseline model, $Re = 4.3 \times 10^6$, $\alpha = 0.0^\circ$, $M = 6.8$.

FIGURE 26: Heat flux comparisons on the tangent-slot model and the baseline model, $Re = 4.3 \times 10^6$, $\alpha = 0.0^\circ$, $M = 6$.

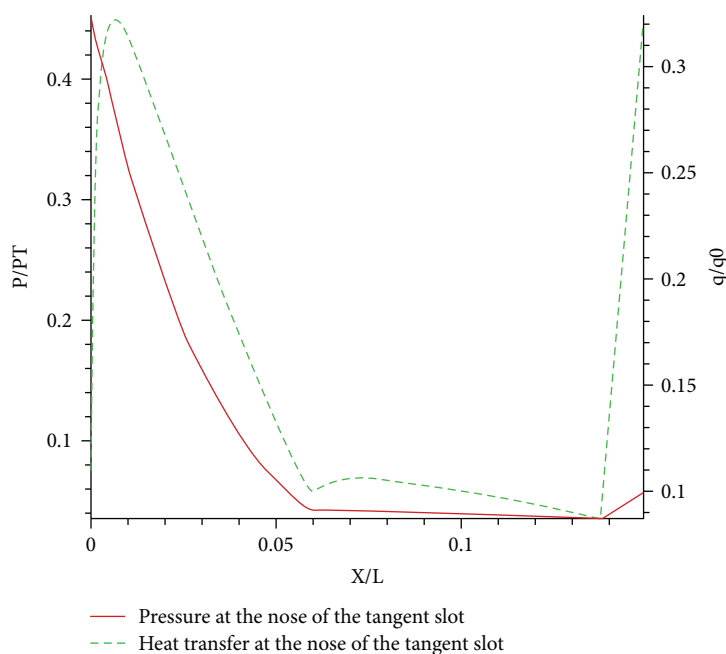


FIGURE 27: Pressure and heat transfer rates near the tangent-slot nose.

the difference in results near the middle of the model, it is clear that the baseline model is well resolved by the present computations. The numerical results for the tangent-slot model are below the measured data up to an Sa/L value of <0.6 ; however, the numerical results do climb steadily towards the experimental data towards the rear of the tangent-slot model. It is duly noted however that the application of tangential blowing does lead to a reduction in the heat transfer rates. It was observed earlier that the jet flow transforms the boundary layer by creating a slow moving cooler layer next to the wall. The difference between the computed and experimental results of the heat transfer is within experimental error bar shown in the figure.

In order to analyze the flow near the nose with no jet application, the pressure distribution P on the surface normalized with respect to the stagnation value PT used earlier, and the heat transfer rates were plotted along an axial distance as shown in Figure 27. There was no experimental data available for the comparison.

The nose pressure value normalized with respect to the stagnation value from R1 drops down from 0.45 to a local P/PT value of about 0.06 as the flow continues to expand around the spherical region. The heat transfer rate drops from a peak high value of about $q/q_0 = 0.325$ very close to the nose to a value of about 0.1 at $X/L = 0.06$. It then increases slightly before dropping down to a $q/q_0 = 0.085$ before witnessing a very sharp at the slot entrance.

7. Conclusion

Normal and tangential blowing has been examined as a means of reducing the blunt body hypersonic heat transfer rates. The computations have shown that there are very well-established regions of flow reversal and separation on

both Gasjet and tangent-slot models. The two-equation models Wilcox $k-\omega$ or the $k-\epsilon$ models may produce reasonable pressure distribution results over the surface of solid bodies or bodies with low surface blowing, but they have been found to be inadequate to resolve more accurate heat flux comparison with experiment. With blowing, the pressure on the boundary surface is carefully modulated to produce a constant flow across the surface. The computations can force a constant outflow condition but cannot adjust the exact pressure profile used in the experiment. This may be the inherent cause in obtaining the exact match between numerical and experimental simulations. However, in terms of validating the jet flow concept alleviation, the results on both models have shown that blowing does lead to a reduction in heat transfer rates on a surface exposed to hypersonic flow. If large mesh requirements were not an impediment, then the application LES (detached eddy simulation) or DES based viscous coupling would be more useful.

Data Availability

The data in our paper is open to use by other researchers.

Disclosure

An earlier version of this paper was presented at the 22nd AIAA International Space Planes and Hypersonic Systems and Technologies Conference.

Conflicts of Interest

The authors declare that there is no conflict of interest regarding the publication of this paper.

Acknowledgments

This work was funded by the Deanship of Scientific Research (DSR), King Abdulaziz University, Jeddah, under the Grant no. 104-135-D1440. The authors, therefore, acknowledge with thanks the DSR for technical and financial support.

References

- [1] L. Lees, "Laminar heat transfer over blunt-nosed bodies at hypersonic flight speeds," *Journal of Jet Propulsion*, vol. 26, no. 4, pp. 259–269, 1956.
- [2] J. A. Fay and F. R. Riddell, "Theory of stagnation point heat transfer in dissociated air," *Journal of the Aerospace Sciences*, vol. 25, no. 2, pp. 73–85, 1958.
- [3] N. B. Cohen, *Boundary-layer similar solutions and correlation equations for laminar heat-transfer distribution in equilibrium air at velocities up to 41,100 feet per second*, Tech. Rep. R-118, National Aeronautics and Space Administration, Washington, DC, USA, 1961.
- [4] L. F. Crabtree, R. L. Dommette, and J. G. Woodley, *Estimation of heat transfer to flat plates, cones and blunt bodies*, Aeronautical Research Council Reports and Memoranda No. 3667, 1965.
- [5] K. C. Chen, "Compressible turbulent boundary-layer heat transfer to rough surfaces in pressure gradient," *AIAA Journal*, vol. 10, no. 5, pp. 623–629, 1972.
- [6] P. G. Cross and I. D. Boyd, "Conjugate analysis of rocket nozzle ablation," in *AIAA Aviation Forum, 47th AIAA Thermophysics Conference*, Denver, Colorado, June 2017.
- [7] L. Zhu, X. Chen, Y. Li, O. Musa, and C. Zhou, "Investigation of drag and heat reduction induced by a novel combinational lateral jet and spike concept in supersonic flows based on conjugate heat transfer approach," *Acta Astronautica*, vol. 142, pp. 300–313, 2018.
- [8] H. Alkandry, I. D. Boyd, E. M. Reed, J. R. Codoni, and J. C. McDaniel, "Interactions of single-nozzle sonic propulsive deceleration jets on Mars entry aeroshells," *Journal of Spacecraft and Rockets*, vol. 48, no. 4, pp. 564–572, 2011.
- [9] P. F. Holloway, J. R. Sterrett, and H. S. Creekmore, *An investigation of heat transfer within regions of separated flow at a Mach number of 6*, Tech. Rep. NASA TN D-3074, 1965.
- [10] J. C. Emery, T. J. Goldberg, and J. W. Keyes, "Turbulent heat transfer associated with control surface at Mach 6," *AIAA Journal*, vol. 6, no. 8, pp. 1612–1613, 1968.
- [11] L. H. Back and R. F. Cuffel, "Changes in heat transfer from turbulent boundary layers interacting with shock waves and expansion waves," *AIAA Journal*, vol. 8, no. 10, pp. 1871–1873, 1970.
- [12] V. G. Candler, M. S. Holder, L. D. Boyd, and W.-L. Wang, "CFD validation for hypersonic flight: hypersonic double-cone flow simulations," in *40th AIAA Aerospace Sciences Meeting & Exhibit, RTO-TR-AVT-007-V3*, Reno, NV, USA, 2006.
- [13] A. Ali Pasha, K. A. Juhany, and M. Khalid, "Numerical prediction of shock/boundary-layer interactions at high Mach numbers using a modified Spalart–Allmaras model," *Engineering Applications of Computational Fluid Mechanics*, vol. 12, no. 1, pp. 459–472, 2018.
- [14] J. T. Howe and W. A. Mersman, "Solutions of the laminar and compressible boundary-layer equations with transpiration which are applicable to stagnation regions of axisymmetric blunt bodies," Technical Note D-12, National Aeronautics and Space Administration, 1959.
- [15] G. M. Low, *The compressible laminar boundary layer with fluid injection*, Tech. Rep. NACA TN 3404, National Advisory Committee for Aeronautics, Washington, DC, USA, 1955.
- [16] C. C. Pappas and A. F. Okuno, *Heat transfer measurement for binary gas laminar boundary layers with high rates of injection*, Technical Note D-2473, National Aeronautics and Space Administration, Washington, DC, USA, 1964.
- [17] C. C. Pappas and A. F. Okuno, *The relation between skin-friction and heat transfer for the turbulent boundary layer on a cone with foreign gas injection*, Technical Note TN D-2857, National Aeronautics and Space Administration, 1965.
- [18] W. H. Dorrance, *Viscous Hypersonic Flow*, McGraw Hill Book Co., Inc, 1962.
- [19] M. E. Tauber, *A review of high speed convective, heat transfer computation methods*, NASA Technical Paper 2914, 1989.
- [20] J. R. Nowak, *Gasjet and tangent slot cooling film tests of a 12.5° Cone at Mach Number of 6.7*, NASA Technical Paper 27866, 1988.
- [21] M. Vinokur, "Conservation equations of gas dynamics in curvilinear coordinate systems," *Journal of Computational Physics*, vol. 14, no. 2, pp. 105–125, 1974.
- [22] R. M. Beam and R. F. Warming, "An implicit finite difference algorithm for hyperbolic systems in conservation law form," *Journal of Computational Physics*, vol. 22, no. 1, pp. 87–110, 1976.
- [23] T. H. Pulliam and D. S. Chaussee, "A diagonal form of an implicit approximate-factorization algorithm," *Journal of Computational Physics*, vol. 39, no. 2, pp. 347–363, 1981.
- [24] J. Zhu and T. H. Shih, *An NPARC turbulence module with wall functions*, NASA Contractor Report 204142 ICOMP-97-09; CMOTT-97-04, AIAA-96–038, 2012.
- [25] R. Grundmann, *Aerothermodynamik*, Springer Verlag, 2000.
- [26] S. Gordon and B. McBride, *Computer program for calculation of complex chemical equilibrium compositions and applications*, Technical report, National Aeronautics and Space Administration, Office of Management, Sciatic and Technical Information Program, 1994.
- [27] M. Khalid and K. A. Juhany, "Hypersonic heat transfer alleviation studies on re entry vehicles," in *AIAA 2017-2266, 21st AIAA International Space Planes and Hypersonic Technologies Conference*, Xiamen, China, 2017.
- [28] M. Khalid and K. A. Juhany, "Heat alleviation studies on hypersonic re-entry vehicles," *Aeronautical Journal*, vol. 122, no. 1257, pp. 1673–1696, 2018.
- [29] B. S. Kirk, "Adiabatic shock capturing in perfect gas hypersonic flows," *International Journal for Numerical Methods in Fluids*, vol. 64, pp. 1041–1062, 2010.
- [30] K. Peery and S. Imlay, "Blunt body flow simulations," in *24th Joint Propulsion Conference, AIAA Paper 2904*, Boston, MA, USA, July 1988.
- [31] F. Ismail and P. L. Roe, "Affordable, entropy-consistent Euler flux functions II: entropy production at shocks," *Journal of Computational Physics*, vol. 228, no. 15, pp. 5410–5436, 2009.
- [32] J. Garicano-Mena, A. Lani, and H. Deconinck, "An energy-dissipative remedy against carbuncle: application to hypersonic flows around blunt bodies," *Computers and Fluids*, vol. 133, pp. 43–54, 2016.

- [33] M. Khalid, A. Dujardin, P. Hennig et al., "Turbulence model studies to investigate the aerodynamic performance of a NASA dual control missile at supersonic Mach numbers," *Canadian Aeronautics and Space Journal*, vol. 51, no. 4, pp. 153–166, 2005.
- [34] R. A. Thompson and P. Gnoffo, "Implementation of a boundary condition in the LAURA code," *46th Aerospace Sciences Meeting and Exhibits*, 2008, Reno NV, USA, January 2008, 2008.



Hindawi

Submit your manuscripts at
www.hindawi.com

